

Synthesis of $\text{SiO}_2/\text{ZnO}/\text{Fe}_2\text{O}_3/\text{ZnFe}_2\text{O}_4$ from Spent Alkaline Batteries and Mining Tailings Applied as a Photocatalyst and Pseudocapacitor

Luma B. Magnago,^{1b}*,^{a,b} Fernando S. Betim,^{1b}^{c,d} Jenifer R. Almeida,^{1b}^a Mayra N. Moura,^{1b}^a
Edson L. D. Coelho,^{1b}^c Vitor M. Leal,^{1b}^c Sandra A. D. Ferreira,^a Maria F. F. Lelis^{1b}^a
and Marcos B. J. G. Freitas^{1b}^c

^aLaboratório de Análise e Tratamento de Água, Departamento de Química,
Universidade Federal do Espírito Santo, Av. Fernando Ferrari, 514, Goiabeiras,
29075-910 Vitória-ES, Brazil

^bInstituto Federal de Educação, Ciência e Tecnologia do Espírito Santo, Rodovia BR-259, km 70,
Distrito de Itapina, 29717-000 Colatina-ES, Brazil

^cLaboratório de Eletroquímica e Eletroanálise, Departamento de Química,
Universidade Federal do Espírito Santo, Av. Fernando Ferrari, 514, Goiabeiras,
29075-910 Vitória-ES, Brazil

^dInstituto Federal de Educação, Ciência e Tecnologia do Espírito Santo,
Rodovia Miguel Curry Carneiro, 799, Santa Luzia, 29830-000 Nova Venécia-ES, Brazil

In this study, a mixed oxide ($\text{SiO}_2/\text{ZnO}/\text{Fe}_2\text{O}_3/\text{ZnFe}_2\text{O}_4$) was prepared using the anode recycled from alkaline batteries and the silt fraction of mining tailings and applied as a photocatalyst under solar irradiation and as a pseudocapacitor. The structure and morphology of the mixed oxide revealed clusters of nanometric particles with rhombic and octahedral shapes. A 2^3 full factorial design was performed to determine the effect of pH, hydrogen peroxide (H_2O_2), and photocatalyst on methylene blue (MB) decolorization. The maximum efficiency was 96%, obtained using 2.35×10^{-5} mol H_2O_2 and 20 mg of photocatalyst at pH 3 for 30 min under solar irradiation. This efficiency remained even after four successive decolorization cycles. Pseudocapacitive properties showed that the mixed oxide exhibited favorable characteristics for application as electrochemical pseudocapacitors due to its high capacitance (87.16 F g^{-1}), energy density (27.24 Wh kg^{-1}) at 524.41 W kg^{-1} of power density, and reversibility (93%). The studied mixed oxide has excellent potential for use in photocatalytic reactions and electrochemical devices, contributing to environmental sustainability and circular economy.

Keywords: alkaline batteries, mine tailings, recycling, sustainable photocatalyst, dye removal, pseudocapacitor

Introduction

The Brazilian National Solid Waste Policy has as its primary objectives the non-generation, reduction, reuse, recycling, treatment, and environmentally adequate disposal of solid waste, in this order of priority and without distinction of waste class.¹ However, recent reports²⁻⁵ indicate that such objectives are far from being met, particularly with regard to reuse and recycling. Batteries represent a worrisome source of waste. Every

year, about 1 billion batteries are sold in Brazil, 6 billion in Japan, and about 8 billion are commercialized in the United States and Europe.² It is estimated that 85% of all batteries used commercially worldwide are alkaline batteries, amounting to 40 billion batteries sold annually.^{3,4} According to the 2021 Brazilian Electronic Waste report published by Green Electron, 53 million tons of electronic waste (also known as e-waste) were incorrectly disposed of worldwide, with Brazil occupying the 5th position in the global ranking. In 2019, the country generated more than 2 million tons of e-waste, less than 3% of which was recycled, representing an alarming problem from an environmental perspective.⁵

*e-mail: luma.magnago@gmail.com

Editor handled this article: Rodrigo A. A. Muñoz (Associate)



Alkaline batteries can be found in most portable electronic devices. After their useful life has ended, these batteries have to be discarded, given that they are non-rechargeable (primary cells). As a consequence, alkaline batteries have to be frequently replaced and are likely to be disposed of incorrectly.^{6,7} Adequate disposal methods include landfilling, incineration, and recycling. Recycling is the only practice that benefits future generations, promotes sustainability, preserves raw materials, reduces environmental pollution, and minimizes risks to human health.^{8,9}

Another problematic waste material is iron ore tailings, a type of solid waste generated during iron processing that has limited reuse potential by the industry. Of the 290 million tons of iron ore tailings generated annually in Brazil, 94.58% is stored in dams, 2.87% is stored in tailing piles, and only 0.003% is reused.¹⁰ In 2015, the Fundão dam in Mariana, Minas Gerais State, collapsed, constituting one of the largest socioenvironmental disasters in Brazilian history.^{11,12} The dam, which was classified as high-risk category III, contained about 45 million m³ of iron ore tailings. Residues released upon the collapse of the dam buried the subdistrict of Bento Rodrigues and left a trail of destruction extending to the coast of Espírito Santo State, impacting 663.2 km of waterways.¹³

A potential solution to the above-mentioned problems lies in combining domestic waste (e.g., spent alkaline batteries) and industrial waste (e.g., mining tailing) for the synthesis of novel materials with multiple functionalities, such as photocatalytic and pseudocapacitive, for example.

Photocatalysis is an efficient, simple, easy, reproducible, cost-effective, and environmentally friendly method to treat wastewater pollution. Photocatalysts used in wastewater treatment are typically semiconductor materials activated by photon absorption. Pollutant degradation occurs in several steps involving oxidizing and reducing species photogenerated on the photocatalyst surface by ultraviolet (UV) or visible (Vis) light. When carried out under solar irradiation, photocatalysis offers additional advantages, as it relies on a renewable, green, and free energy source.¹⁴⁻¹⁷

Hematite (Fe₂O₃) and zinc oxide (ZnO) have attracted great attention in water treatment as photocatalysts in dye degradation reactions.¹⁸⁻²⁴ Fe₂O₃ has a band gap of 2.1 eV, with absorption in the visible region at 564 nm, allowing the collection of about 40% of the photons from sunlight. Natural abundance, low-cost synthesis, non-toxicity, excellent chemical stability, and environmental friendliness are other prominent characteristics of Fe₂O₃.^{16,25} ZnO, with a band gap of 3.2 V, excels in terms of catalytic activity and photocatalytic degradation owing to its high electron mobility.²⁶ In addition, the semiconductor oxides

Fe₂O₃ and ZnO also exhibit good electrochemical activity and have been studied for use in supercapacitors due to their pseudocapacitive behavior, high energy density, and efficiency.^{27,28} Supercapacitors belong to the class of electrochemical energy storage devices which offers high energy and power density with long cyclic stability.^{29,30}

Several studies reported the synthesis of Fe₂O₃ and ZnO from commercial reagents, such as nitrates,³¹ chlorides,³² and acetates.³³ In the current study, Fe₂O₃ was recovered from iron ore tailings and ZnO was recycled from the anode of spent alkaline batteries. The materials were used to produce a robust, economical, non-toxic, easily accessible, and highly photoactive mixed oxide for use as a photocatalyst in the removal of MB dye under solar irradiation and for use as an electrochemical energy storage device. By combining industrial and domestic waste for the preparation of a bifunctional material, this article presents a comprehensive solution that adds value to waste materials, reduces the need for raw materials, and contributes to a circular economy.

Experimental

Materials

All chemicals were of reagent grade and used as received unless otherwise specified. Citric acid (C₆H₈O₇) and potassium hydroxide (KOH) were purchased from Dinâmica (Indaiatuba, Brazil). Ammonium hydroxide (NH₄OH) (28-30%), methylene blue (MB) dye, H₂O₂ (35%), and isopropyl alcohol (C₃H₈O) were purchased from Neon (Suzano, Brazil). Carbon black VXC72 (Boston, USA) was purchased from Cabot. Carboxymethyl cellulose (CMC) was purchased from Êxodo Científica (Sumaré, Brazil). NafionTM and hydrochloric acid (HCl) (37%) were purchased from Sigma-Aldrich (St. Louis, USA). Sodium hydroxide (NaOH) was purchased from Vetec (Duque de Caxias, Brazil). Hydrochloric acid and sodium hydroxide were used as 0.1 mol L⁻¹ solutions for pH adjustments.

Dismantling and recovery of anode material from spent alkaline batteries

Spent alkaline batteries were completely discharged, manually dismantled, and separated into basic components (plastic casing, separator, current collector, cathode, and anode). The anode material was washed with 0.1 mol L⁻¹ citric acid and deionized water until pH 7 was achieved. This step cleans and removes the KOH electrolyte from the anode. Then, the anode material was oven-dried (404/D, Nova Ética, Brazil) at 80 °C for 24 h and ground using

an agate mortar and pestle for particle size reduction and homogenization.

Collection and processing of mining tailing samples

Mining tailing samples were collected at the tailing landfill of Fazenda Floresta, close to the dam of the Risoleta Neves Hydroelectric Power Plant (Candonga Power Plant). Figures S1a and S1b (Supplementary Information (SI) section) show the landfill and the five points selected for sample collection. Two samples were collected from each sampling point, one from the surface and one at 1 m depth, totaling 10 samples. Collections were performed by the Candonga Project team and followed the recommendations of ABNT NBR 10007:2004.³⁴ According to Figueiredo *et al.*³⁵ the tailings meet the criteria of the cited norm for Class II B solid waste (non-hazardous and inert).³⁶ Samples were processed according to the steps of the Brazilian Agricultural Research Corporation (EMBRAPA) sample processing procedure, as follows: spreading, declumping, drying, sieving, quartering, grinding, and storage.³⁷

Separation of tailing fractions

For separation of the sand fraction, a 25.00 g aliquot of the tailing sample was weighed and transferred to a 400 mL beaker containing 100 mL of NH₄OH, pH 10. Then, the sample was subjected to ultrasonic dispersion for 10 min in an ultrasound bath (UltraCleaner 1400A, Unique, Brazil). The suspension was allowed to stand at room temperature (25 °C), causing sedimentation of the sand fraction at a rate of 4 s cm⁻¹. The mixture was passed through a 0.053 mm sieve to separate the sand fraction from silt and clay fractions. The suspension containing silt and clay was collected into a 600 mL beaker. The sediment (sand fraction) was stored.

For separation of silt and clay fractions, the aforementioned suspension was transferred to a 1000 mL beaker and the volume was completed with NH₄OH solution, pH 10. The system was shaken vigorously and allowed to stand. The clay fraction was separated from the silt fraction by periodic siphoning (every 12 h), while the pH was maintained at 10 by the addition of NH₄OH solution. The process was repeated until the suspension became clear, indicating that the entire clay fraction had been separated from the silt fraction. The suspension containing the clay fraction was stored. The sediment containing the silt fraction was oven-dried at 110 °C, weighed, and stored for use in the preparation of the mixed oxide. The silt content of the mining tailing sample was

44.8% m m⁻¹. We decided to use the silt fraction rather than the whole mining tailing sample because it contains higher amounts of iron and lower amounts of silica.

Preparation of the mixed oxide from alkaline battery anode and the silt fraction of mining tailings

The mixed oxide was prepared by mixing 1.47 g of the silt fraction (8.29 mmol Fe) of mining tailings with 0.489 g of alkaline battery anode material (4.15 mmol Zn) and 1.0 g of CMC. CMC was used to produce a reducing atmosphere during calcination, which is important for the formation of the crystalline phase. After weighing, the materials were grounded and homogenized using an agate mortar and pestle and calcined in porcelain crucibles at 800 °C for 3 h. The muffle furnace (LF00212, Jung, Blumenau, Brazil) was heated at a rate of 4.4 °C min⁻¹. The calcined material was washed with distilled water and oven-dried at 80 °C for 24 h. The calcination step eliminates undesired components (water, volatiles, unstable ions, among others) and stabilizes the crystalline structure.

Full factorial design experiments

To minimize costs and operational time, we used a 2³ full factorial design to identify the best conditions for decolorization of 25.00 mL of 20 mg L⁻¹ MB solution (1.56 × 10⁻⁶ mol). The following three independent variables were studied: pH, H₂O₂ concentration, and catalyst (mixed oxide) mass. Each factor was tested at two levels, coded as -1 (low level) and +1 (high level). A full factorial design provides insight into the effects of operational variables and their interactions for process optimization. Factors and their levels (real and coded values) are presented in Table 1.

Table 1. Levels of a 2³ full factorial design

Independent variables	Coded and actual levels	
	(-1)	(+1)
pH	3	7
H ₂ O ₂ / (×10 ⁻⁵ mol)	2.35	4.70
Mixed oxide / mg	20	40

All combinations of all factors in Table 1 resulted in 8 runs. Therefore, decolorization tests were performed in 100 mL beakers under solar irradiation with the conditions listed in Table S1 (SI section). No apparatus was employed in the experiment, only the beakers with the listed conditions and sunlight.

Aliquots were collected at 0, 15, 30, 45, 60, and 90 min for absorbance measurements using a UV-Vis

spectrophotometer (HACH, DR5000, Ames, USA) at 665 nm. The response (dependent variable) was decolorization efficiency, calculated using equation 1.

$$\text{Decolorization efficiency (\%)} = \left(\frac{A_0 - A}{A_0} \right) \times 100 \quad (1)$$

where A_0 and A are the initial and final absorbances of MB solution, respectively.

Experimental data were analyzed using Statistica trial version 11.0.³⁸

Temperature, solar irradiation, and rainfall data for the days when the tests were conducted are presented in Table S2 (SI section). The temperature remained relatively constant, there was no rainfall, and solar irradiation reached a peak at 3 p.m. Meteorological data were collected by the automatic weather station of Vitória, Espírito Santo, Brazil, located about 1 km from the municipality.

Additional tests were performed with pH at five levels (pH 3-7). Reactions were conducted using 1.56×10^{-6} mol MB, 2.35×10^{-5} mol H₂O₂, and 20 mg of mixed oxide for 30 min under solar irradiation. The results were used to construct a mathematical model describing the dependent variable as a function of significant variables ($p < 0.05$). Analysis of variance (ANOVA) was used to assess the goodness of fit of the model to experimental results.

Pre-saturation of the mixed oxide with the dye before photocatalysis was unnecessary, as preliminary tests indicated that the dye is not adsorbed by the mixed oxide, as shown in Figure S2 (SI section).

Photocatalytic study and reusability assessment of the mixed oxide under optimal conditions

A study of four reaction systems was carried out to better understand the effects of each reaction component on the photocatalytic process. Reactions were prepared in 100 mL beakers and conducted under optimal conditions obtained through the 2³ full factorial design. Systems were as follows: (1) 1.56×10^{-6} mol MB, (2) 1.56×10^{-6} mol MB + 20 mg of mixed oxide, (3) 1.56×10^{-6} mol MB + 2.35×10^{-5} mol H₂O₂, and (4) 1.56×10^{-6} mol MB + 2.35×10^{-5} mol H₂O₂ + 20 mg of mixed oxide. MB solutions had an initial pH of 3, were kept under solar irradiation, and were analyzed spectrophotometrically at times 0, 5, 10, 15, 20, 25 and 30 min. The experiments were conducted in triplicate. The mixed oxide used in system 4 was filtered, washed with distilled water, dried at 80 °C for 24 h, and reused in successive catalytic cycles under optimal conditions.

Preparation of the composite, working electrodes, and electrochemical cell

Initially, a composite was prepared containing the electroactive material (mixed oxide) and carbon black in a mass ratio of 90:10. For the composite preparation, a mass of 9.004 mg of the mixed oxide and 1.173 mg of carbon black was dispersed in a solution of 400 μL of isopropyl alcohol and 100 μL Nafion™, resulting in a solid/liquid ratio of 10 mg *per* 500 μL. Then, the system was subjected to sonication for 90 min.

For the preparation of the working electrode, a glassy carbon substrate with a geometric area of 0.073 cm² was used. Onto the substrate, 5 μL of the composite was added through two additions of 2.5 μL each. Then, the electrode was dried at a temperature of 60 °C in an oven for a period of 24 h.

For the electrochemical tests, the conventional three-electrode system was employed: a mixed oxide composite electrode as the working electrode, a platinum wire as the counter electrode, and an Hg/HgO electrode as the reference electrode. All measurements were conducted in a 1.0 mol L⁻¹ KOH electrolyte.

Cyclic voltammetry tests using potentiostatic scanning

The cyclic voltammetry tests using potentiostatic scanning were performed starting from the open circuit potential of -0.12 V (initial E = -0.12 V) with an initial anodic scan up to a potential of 0.75 V, followed by a cathodic scan back to -0.75 V. A study of the scan rate was conducted using the values of 150, 125, 100, 75, 50, 25 and 10 mV s⁻¹.

Galvanostatic charge/discharge tests

The tests were conducted using the galvanostatic charge/discharge chronopotentiometry method. During the charge process, a constant current of 6.3028×10^{-5} A was applied until reaching a potential of 0.75 V. Subsequently, a current of -6.3028×10^{-5} A was applied during the discharge process until reaching a potential of -0.75 V. The charging time and discharging time were monitored.

The current (I) of 6.3028×10^{-5} A was determined based on the current density relationship (equation 2).

$$J = \frac{I}{m} \quad (2)$$

where J is the current density (0.7 A g⁻¹) and the m is the mass of the mixed oxide (9.004×10^{-2} mg).

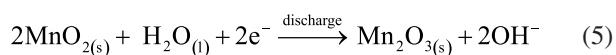
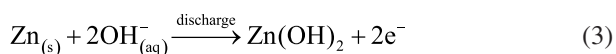
Characterization techniques

X-ray diffractometry (XRD) analyses were conducted using a diffractometer (Bruker, D8 DISCOVER, Billerica, USA) with Cu K α radiation ($\lambda = 1.540598 \text{ \AA}$) in the 2θ range of 10 to 90° at a scanning rate 1° min^{-1} . Scanning electron microscopy (SEM) was performed using a microscope (Shimadzu, SUPERSCAN SSX-550, Kyoto, Japan) with an accelerating voltage of 20.0 kV and magnifications of $500\times$ ($50 \text{ }\mu\text{m}$) and $2000\times$ ($10 \text{ }\mu\text{m}$). Energy-dispersive X-ray spectroscopy (EDX) analyses were conducted using an energy detector (Bruker, XFlash[®] Detector 6110, Billerica, USA) coupled to the SEM. Transmission electron microscopy (TEM) was performed using a microscope (JEOL, JEM1400, Akishima, Japan) equipped with a LaB₆ filament with magnifications of 200 and 100 nm . Inductively coupled plasma optical emission spectrometry (ICP-OES) was performed using a spectrometer (PerkinElmer, Optima 7000 DV, Waltham, USA) with intensity measured in area mode, employing axial view for analysis. The gases employed were as follows: argon with 99.999% purity (Oxivit, Serra, Brazil) for the plasma gas; compressed air passed through two humidity filters for the auxiliary gas, and nitrogen with 99.999% purity (Oxivit, Serra, Brazil) for the nebulizer gas.

Results and Discussion

Characterization of alkaline battery anode by XRD and ICP-OES

In alkaline batteries, the anode contains metallic zinc and the cathode contains MnO₂. In the anodic discharge reaction, which produces energy, metallic zinc is oxidized to Zn(OH)₂ (equation 3) and/or ZnO (equation 4) in the presence of KOH electrolyte.³⁹ In the cathodic reaction (equation 5), MnO₂ is reduced to Mn₂O₃. The XRD patterns of the alkaline battery anode are presented in Figure S3 (SI section). The diffractogram shows characteristic and well-defined peaks of ZnO (PDF 00-036-1451). The sole presence of ZnO peaks indicates that this is the major phase of the anode material.



ICP-OES analyses were performed to determine the elemental composition of the anode

material. The results revealed the anode contains Zn ($55.45 \pm 5.38\%$) m m^{-1} , Mn ($0.0072 \pm 0.0011\%$) m m^{-1} , and Fe ($0.00068 \pm 0.0004\%$) m m^{-1} . Belardi *et al.*⁴⁰ analyzed the anode of alkaline batteries and found a Zn mass concentration of 53.86% m m^{-1} . Valdez *et al.*⁴¹ reported a Zn concentration of 42% m m^{-1} , whereas Cabral *et al.*⁴² and Almeida *et al.*⁴³ found values greater than 60% m m^{-1} . These discrepancies in results may be related to changes in battery manufacturing throughout the years, differences between battery brands, or differences in the number of batteries analyzed and pre-treatment procedures (e.g., electrolyte removal) used between studies. Of note, the low Mn percentage detected here indicates possible contamination of the anode by the cathode during the dismantling procedure.

Characterization of the silt fraction of mining tailings by XRD and ICP-OES

The diffractogram of the silt fraction of mining tailings (Figure S4, SI section) shows the presence of quartz (SiO₂) (PDF 01-086-1630) and Fe₂O₃ (PDF 00-024-0072) phases. Almeida *et al.*⁴⁴ also identified a kaolinite (Al₂Si₂O₅(OH)₄) phase. In the current study, however, peaks relative to this phase might have been masked by the high intensity of SiO₂ peaks.

To complement XRD characterization results, we determined the chemical composition of the silt fraction by ICP-OES. The silt fraction was found to contain Fe ($31.49 \pm 0.40\%$) m m^{-1} and Al ($0.367 \pm 0.005\%$) m m^{-1} . These small amounts of Al may be related to the presence of mineral kaolinite, which was reported by Almeida *et al.*⁴⁴ and could not be detected by XRD in the current study. Other elements, such as Zn, Mn, and Cu, were not detected, likely being present at concentrations below the limit of detection of the equipment.

Characterization of the mixed oxide by XRD, ICP-OES, SEM/EDX, and TEM

Figures 1a-1c present the XRD, SEM, and TEM results, respectively, of the mixed oxide. Comparison with PDF data allowed us to identify peaks relative to SiO₂ (PDF 01-087-2096), Fe₂O₃ (PDF 01-073-2234), ZnO (PDF 00-036-1451), and franklinite (ZnFe₂O₄) (PDF 01-074-2397) phases in the diffractogram of Figure 1a. The SiO₂ and Fe₂O₃ phases were expected, as they had been identified in the diffractogram of the silt fraction (Figure S4, SI section), as well as the ZnO phase, which was present in the diffractogram of the anode material (Figure S3, SI section). The new phase, ZnFe₂O₄,

has a lower band gap energy (1.9 eV) than Fe_2O_3 (2.1 eV) and ZnO (3.2 eV). This property facilitates photogeneration of the electron-hole pair and increases the efficiency of photocatalytic decolorization.⁴⁵

The micrographs of Figure 1b depict the morphology of the material at high resolutions. Both micrographs display clusters of particles of varying shapes and sizes and absence of pores on particle surfaces. The micrographs of Figure 1c reveal clusters of particles of varying sizes and irregular shapes, with nanometric dimensions and rhombus/octahedral configuration (red arrows).

The EDX map of Figure 2 shows the distribution of elements on the surface of the mixed oxide. Fe, Zn, and O were homogeneously distributed. In the Si map, the lack of gray color indicates low SiO_2 concentration on the surface of the mixed oxide. Au, C, and Al are present. The presence of Au is attributed to metallization during sample preparation, Al is found in the substrate, and C composes the sample holder.

ICP-OES was performed to obtain more information on material composition. The results indicated the presence of Fe ($49.31 \pm 0.99\%$) m m^{-1} , Zn ($20.20 \pm 0.21\%$) m m^{-1} , Al ($1.69 \pm 0.01\%$) m m^{-1} , and Mn ($0.06 \pm 0.0004\%$) m m^{-1} . As performed by Cherpin *et al.*,⁴⁶ powdered reagents were mixed using mortar and pestle before heat treatment; therefore, it was expected that the mixed oxide would contain other elements, even if at low concentrations, such as Al from the kaolinite phase of tailings and Mn from the alkaline battery, as evidenced by ICP-OES of the battery.

Determination of significant effects on MB decolorization

Figure S5 (SI section) shows the results of the eight runs of the 2^3 experimental design. Equilibrium was reached first in runs 1, 3, 5, and 7, within 30 min. This time was used for statistical analyses. Figure S6 (SI section) depicts the Pareto chart for the 30 min reaction.

Pareto charts are used to identify the variables and

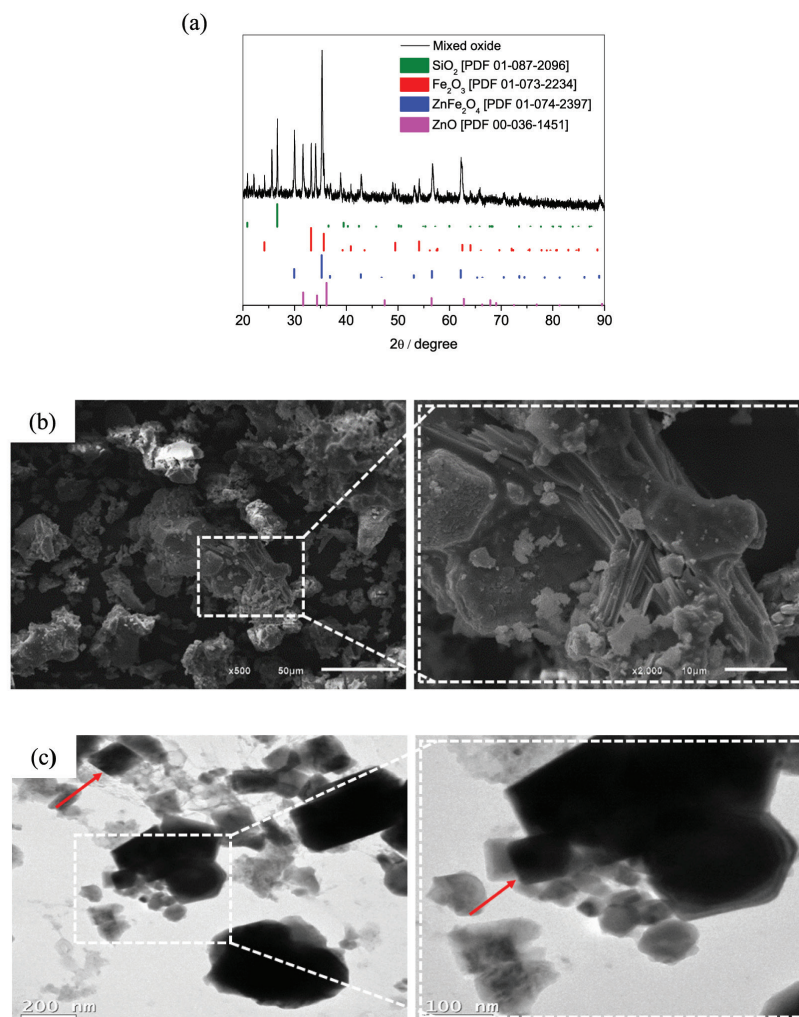


Figure 1. (a) XRD of the mixed oxide, showing assigned phases (SiO_2 , Fe_2O_3 , ZnFe_2O_4 and ZnO), (b) SEM, and (c) TEM analysis of the mixed oxide, showing clusters of particles of varying sizes and irregular shapes.

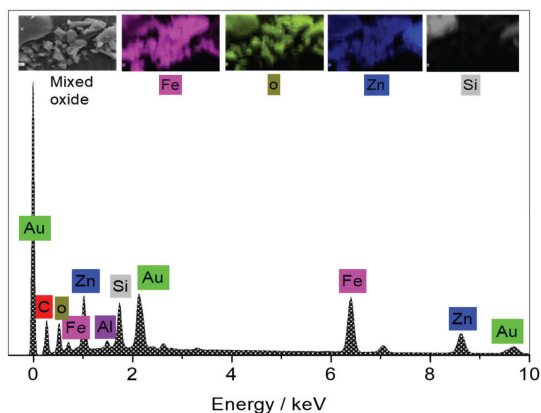


Figure 2. EDX map of the mixed oxide showing the distribution of elements on the material's surface.

interactions that are significant. The effects of each variable and interaction appear in order of significance ($p = 0.05$, dotted red line). Effects that cross the line are considered significant and those that do not cross the line are considered non-significant.⁴⁷ The chart shows that only the effect of H₂O₂ × mixed oxide was not significant. A non-significant effect indicates that, within the studied range, the highest or lowest level of the variable can be chosen without having significant effects on the results.

pH was the variable that exerted the most significant effect (-731.42) on the 30 min reaction. The effect was negative, indicating that a lower pH increases MB decolorization. The variables H₂O₂ and mixed oxide had effects of 40.21 and -23.07 , respectively, indicating that decolorization is enhanced by a high H₂O₂ content and low mixed oxide content.

Response surface and contour plots were constructed to better visualize the effects of the studied variables (Figure 3).

Figures 3a and 3b confirm the importance of pH for decolorization efficiency. The highest efficiencies are obtained at lower pH values. H₂O₂, by contrast, does not provide such significant changes to decolorization efficiency when an acidic pH is used. The interaction effect of mixed oxide and H₂O₂ (Figures 3c and 3d) had little influence on the system (small variation of 68-72%) compared with pH. Figure 3d shows that the highest decolorization efficiency is obtained by using the lowest levels of H₂O₂ (2.35×10^{-5} mol) and mixed oxide (20 mg). Figures 3e and 3f reinforce the high influence of pH on the studied process and de low influence of the mixed oxide.

Given that the effect of H₂O₂ was not as significant as that of pH in the 30 min reaction, the following assays were carried out using the low level of H₂O₂ (2.35×10^{-5} mol) and mixed oxide (20 mg). For pH, it was not possible to determine the optimal value from Pareto, response surface, and contour plots, necessitating optimization experiments.

Determination of the optimal pH for MB decolorization and model proposal

Figure S7 (SI section) presents the optimization graph of pH (five levels) as a function of decolorization efficiency and equation 6 presents the proposed quadratic model (valid for pH values of 3 to 7). The quality of the proposed model was assessed by ANOVA, and the results are described in Table 2.

$$\text{Decolorization efficiency (\%)} = 232.87 - 60.25\text{pH} + 4.48 \text{pH}^2 \quad (6)$$

The coefficient of determination (R^2) of 0.9925 indicates that 99.25% of the total sum of squares (SST) refers to the fraction described by between sum of squares (SSB) and only 0.75% corresponds to the fraction of within sum of squares (SSW). The high R^2 value indicates an optimal fit of the model to the data. At the 95% confidence level, the F -critical for 2 and 3 degrees of freedom is 19.16. The F -value for the same degrees of freedom is 198.90, about 10 times higher than the F -critical. This finding shows that the model is reliable and can be used to make predictions about decolorization efficiency as a function of pH.

Kinetics of MB decolorization catalyzed by mixed oxide under optimal conditions

Figures 4a-4c depict the decolorization efficiency, kinetics of decolorization, and resulting solutions, respectively, after 30 min of reaction under optimized conditions.

System 1, containing dye only, and system 2, containing dye and catalyst, afforded the lowest decolorization efficiencies, $2.07 \pm 0.06\%$ and $3.40 \pm 0.04\%$, respectively (Figure 4a). It can be inferred that solar irradiation alone is not sufficient to decolorize MB, not even in the presence of mixed oxide, as is the case of system 2. System 3, composed of the dye solution and H₂O₂, afforded a higher decolorization efficiency ($15.18 \pm 0.09\%$).

The importance of the catalyst is made evident by the results of system 4 (Figure 4a). The decolorization efficiency increased to $96.21 \pm 0.12\%$ after 30 min of reaction. The zero-order kinetic equation (equation 7) provided the best linear fit to the data of Figure 4b.

$$A_0 - A = kt \quad (7)$$

where A is the absorbance at time t and k is the rate constant.

The rate constants of systems 1 and 2 were 0.0008 and 0.0011 mg L⁻¹ min⁻¹, respectively. There was an improvement in the rate constant of system 3 (0.0054 mg L⁻¹ min⁻¹), and system 4 had the highest

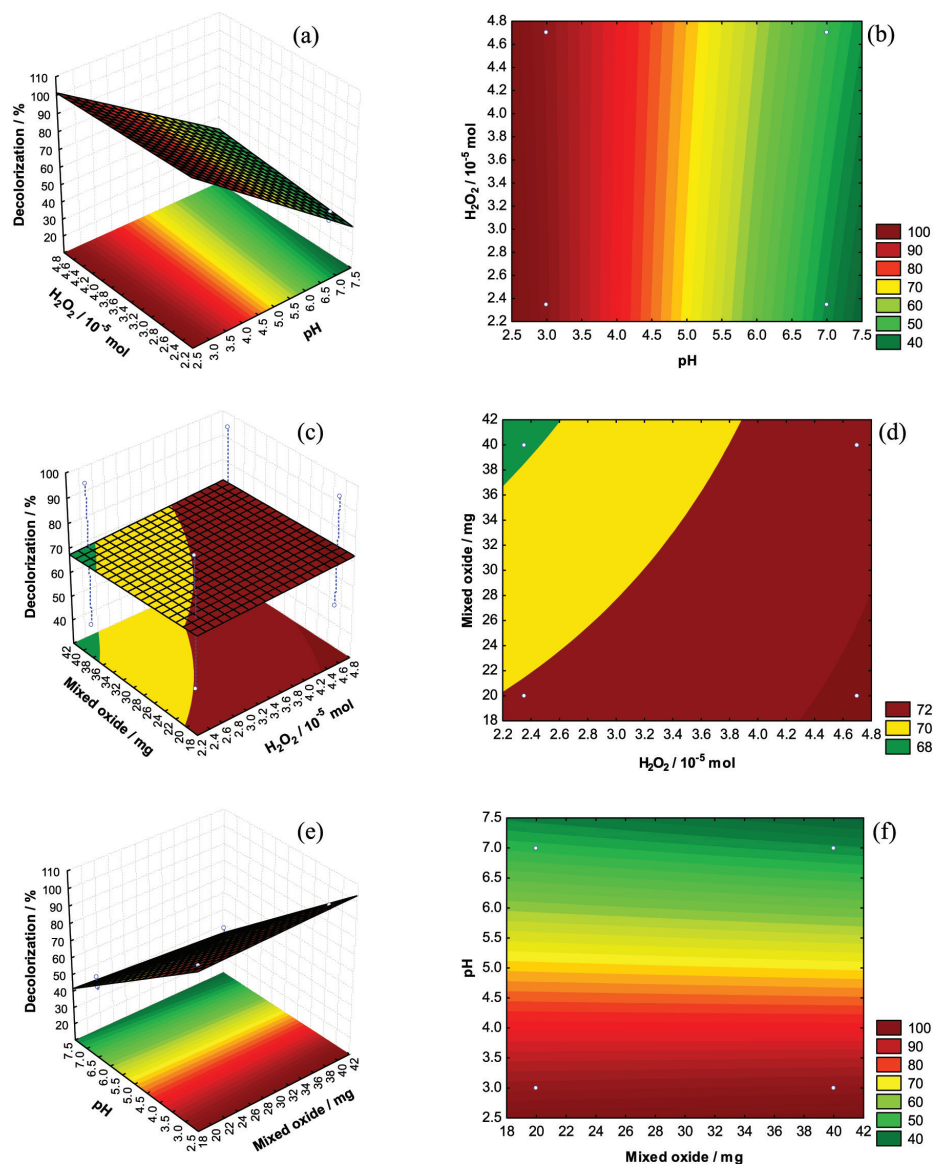


Figure 3. (a) Response surface and (b) contour plot of the variables H₂O₂ and pH, (c) response surface and (d) contour plot of the variables mixed oxide and H₂O₂, (e) response surface and (f) contour plot of the variables pH and mixed oxide.

Table 2. ANOVA for the proposed model in equation 6

Source of variation	Sum of squares (SS)	Degrees of freedom	Mean squares (MS)	R ²	F
Between (B)	$SSB = \sum_{i=1}^n (\hat{y}_i - \bar{y})^2 = 2661.55$	$p - 1 = 2$	$MSB = \frac{SSB}{p - 1} = 1330.77$	$R^2 = \frac{SSB}{SST} = 0.9925$	$F = \frac{MSB}{MSW} = 198.90$
Within (W)	$SSW = \sum_{i=1}^n (y_i - \hat{y}_i)^2 = 20.07$	$n - p = 3$	$MSW = \frac{SSW}{n - p} = 6.69$		
Total (T)	$SST = \sum_{i=1}^n (y_i - \bar{y})^2 = 2681.62$	$n - 1 = 4$			

\hat{y}_i : expected response, \bar{y} : average (mean) of experimental responses, y_i : experimental response, p : number of coefficients, n : number of experiments.

constant (0.0333 mg L⁻¹ min⁻¹). The half-life ($t_{1/2}$), calculated by equation 8, was 697.50, 516.77, 97.86 and 15.85 min for systems 1, 2, 3, and 4, respectively. The

presence of H₂O₂ and catalyst was essential for obtaining a faster and, consequently, more efficient MB decolorization under the proposed conditions.

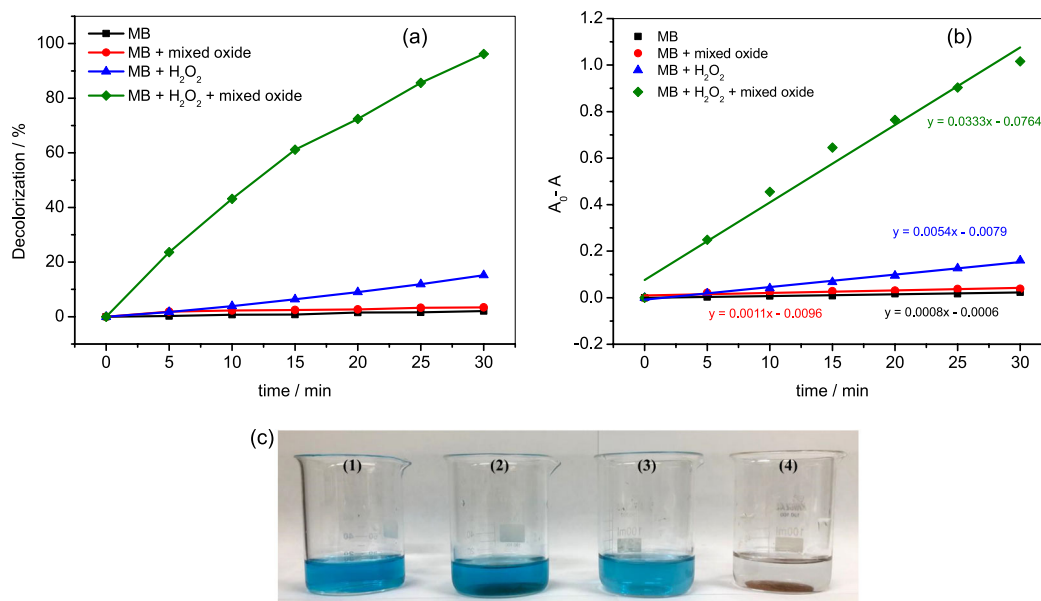


Figure 4. (a) Decolorization as a function of time, (b) zero-order decolorization kinetics and (c) resulting solutions after 30 min under solar irradiation. Conditions: (1) 1.56×10^{-6} mol of MB, (2) 1.56×10^{-6} mol of MB + 20 mg of mixed oxide, (3) 1.56×10^{-6} mol of MB + 2.35×10^{-5} mol of H₂O₂, and (4) 1.56×10^{-6} mol of MB + 2.35×10^{-5} mol of H₂O₂ + 20 mg of mixed oxide, pH 3.

$$t_{1/2} = \frac{A_0}{2k} \quad (8)$$

Similarly to this study, Yildiz *et al.*⁴⁸ in the degradation of Acid Orange 7 using $\text{FeSO}_4 \cdot 7\text{H}_2\text{O}$ and H₂O₂ in a Fenton process, and by Azizi *et al.*⁴⁹ (enhanced Fenton process) and Vianna and Tôrres⁵⁰ (using a $\text{TiO}_2/\text{H}_2\text{O}_2/\text{UV}$ combined process) in the degradation of the azo dye Acid Red 18, found the same zero-order reaction in their degradation processes.

As shown in Figure 4c, the resulting solutions of systems 1-3 had an intense blue color, whereas that of system 4 did not have a blue color, further demonstrating the efficiency of the process. The final pH of system 4 after the decolorization assay was 5.8, not necessitating an adjustment before disposal. The pH range allowed for wastewater disposal is 5 to 9, as determined by Brazilian environmental legislation.⁵¹ The increase in pH after photocatalysis (from 3 to 5.8) may be associated with the formation of weak organic acids from the MB dye molecule. Some authors⁵²⁻⁵⁴ have reported the formation of formic acid, acetic acid, oxalic acid, and propionic acid, as well as nitrate, ammonium, and sulfate ions. Other byproducts and intermediates have also been mentioned, such as phenolic compounds, which are aromatic organic compounds with low biodegradability and high toxicity, posing potential risks to human and environmental health. Therefore, the use of effective methods such as advanced oxidation processes, like photocatalysis, is necessary for the treatment of these compounds.⁵²⁻⁵⁶

Reuse of mixed oxide

Figure 5 presents the reuse performance of the mixed oxide over five cycles of MB decolorization. The conditions were the same in all cycles (1.56×10^{-6} mol dye, 2.35×10^{-5} mol H₂O₂, 20 mg of mixed oxide, pH 3, 30 min, solar irradiation). The decolorization efficiency remained about the same for four cycles, being 95.18, 97.63, 95.71, 96.72% in cycles 1, 2, 3, and 4, respectively. After the 5th cycle, the decolorization efficiency decreased to 83.35%. Such a decrease in efficiency can be attributed to loss of the material during catalyst filtering, washing, and drying for use in subsequent cycles and/or, as stated by Gao *et al.*⁵⁷ to passivation of the catalyst surface with increasing number of cycles. The maintenance of efficiency during the first four cycles demonstrates that the mixed oxide has high stability and can be reused and applied in a practical way for the treatment of textile wastewater.

The reuse capacity of different photocatalysts for dye degradation is shown in Table 3.

Compared with the results of Silva *et al.*⁵⁸ here, the same amount of MB (3.90×10^{-5} mol) was decolorized using 500 mg of the catalyst and 5.88×10^{-4} mol H₂O₂ in just 30 min. Even after four successive cycles, the catalyst would afford a 96% removal of the dye in the last cycle. Silva *et al.*⁵⁸ used 250 mg of the catalyst to achieve 100% efficiency after four cycles, a two times lower weight than that used here. However, the reaction time was 270 min, 9 times longer period, and the H₂O₂ concentration was 2.21×10^{-3} mol, a 3.8 times higher concentration. Another important factor is

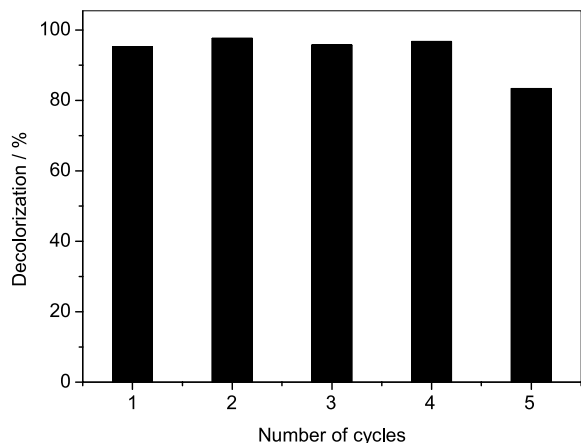


Figure 5. Decolorization of successive cycles with the mixed oxide. Conditions: 1.56×10^{-6} mol of MB, 2.35×10^{-5} mol of H₂O₂, 20 mg of mixed oxide, pH 3, and 30 min under solar irradiation.

that Silva *et al.*⁵⁸ injected air (0.5 L min⁻¹) into the solution for 4 to 6 h before the reaction, a step that was not necessary in the present study. The injection of air into the solution facilitates the generation of additional radicals as hydroxyl radical (HO•) and superoxide radical (O₂•⁻), which contribute to the degradation process (see “Reactions involved in the photocatalytic process” sub-section).

In comparison with the reaction carried out by Ivanets *et al.*⁵⁹ here, the same efficiency was achieved using 12.5 times less catalyst and 42.5 times less H₂O₂. The cited study saturated the catalyst with MB solution (100 mg L⁻¹) for 30 min before the reaction and used a diode as a source of Vis and UV-C lamps as a source of UV radiation, not solar irradiation, as was used here.

Broadly speaking, to treat 1000 L of wastewater containing 20 mg L⁻¹ MB at pH 3 with about 96% efficiency, it would be necessary to use 800 g of the mixed oxide catalyst, 0.94 mol H₂O₂, and 30 min of reaction under solar irradiation. The catalyst could be reused up to four times without losing efficiency. Of note, the catalyst was prepared from tailings of the mining industry and the anode of a spent alkaline battery, representing a sustainable and technological use of wastes that would otherwise cause damage to the environment.

Table 3. Efficiency of photocatalyst reuse in dye decolorization

Reference	Dye		Catalyst		Parameter		Reusability	
	Name	Quantity / mol	Type	Mass / mg	H ₂ O ₂ / mol	pH	Efficiency / %	time in last cycle / min
This work	MB	1.56×10^{-6}	SiO ₂ /ZnO/Fe ₂ O ₃ /ZnFe ₂ O ₄	20	2.35×10^{-5}	3	96 (4 th cycle)	30
45	Rhodamine B	1.04×10^{-5}	ZnFe ₂ O ₄ /Biochar(1:1)	100	1.47×10^{-3}	3	65 (8 th cycle)	60
58	MB	3.90×10^{-5}	α-Fe ₂ O ₃ /CuFe ₂ O ₄	250	2.21×10^{-3}	6	100 (4 th cycle)	60
59	MB	1.56×10^{-6}	MgFe ₂ O ₄ doped with La	250	10 ⁻³	6	90 (4 th cycle)	270
60	MB	2.19×10^{-6}	CoO/ZnO	100	1.06×10^{-2}	6	66.54 (4 th cycle)	180

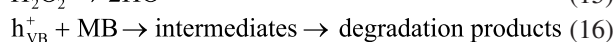
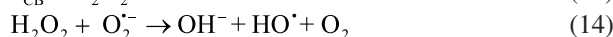
MB: methylene blue.

Reactions involved in the photocatalytic process

The mixed oxide used in this study consists of the semiconductors SiO₂, ZnO, Fe₂O₃, and ZnFe₂O₄. When a semiconductor is excited with photons with sufficient energy, from sunlight for example, an electron-hole pair is formed on its surface. That is, electrons are conducted into the conduction band (e⁻_{CB}), generating holes in the valence band (h⁺_{VB}), as shown in equation 9. h⁺_{VB} may react with water molecules (equation 10) or hydroxyl anions (HO⁻) (equation 11) to form the highly oxidizing HO•. In the conduction band, e⁻_{CB} can react with oxygen to form O₂•⁻, which reacts with hydrogen ions (H⁺) to form hydroperoxyl radical (HOO•) (equation 12). According to Casbeer *et al.*⁶¹ HOO• decomposes rapidly into HO•, a species with higher oxidation potential (E = 2.80 V), exhibiting high reactivity and low selectivity, serving as the primary radical responsible for the degradation process. In this band, HO• radicals are formed through the reaction of the electron with H₂O₂ (equation 13). In addition to these pathways, HO• can also be formed from H₂O₂ and O₂•⁻ (equation 14). In the presence of UV light, the H₂O₂ decomposes into two HO•, enhancing the process efficiency (equation 15). However, it is important to note that the degradation efficiency of a dye or any organic pollutant is negatively affected by excess H₂O₂.⁶² A high H₂O₂ concentration potentiates undesirable reactions involving HO• sequestration. Finally, h⁺_{VB}, given their high oxidative potential, can promote direct oxidation of the organic pollutant (MB) (equation 16), or oxidation can occur via reaction with HO• (equation 17).^{16,62,63}

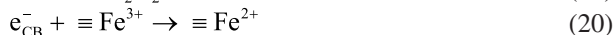


where Cat = SiO₂, ZnO, Fe₂O₃, and ZnFe₂O₄



HO[•] + MB → intermediates → degradation products (17)

When iron is present on the surface of the catalyst (≡Fe), Fenton reactions (equations 18-20) occur concomitantly with the above-mentioned reactions.⁶⁴



Cycling of the Fe²⁺/Fe³⁺ pair (equations 18-20) is critical for the continuity of Fenton reactions and for enhanced process efficiency.⁶⁴

Finally, by establishing a correlation with the kinetic study that demonstrated zero-order kinetics and considering the optimization studies, it can be affirmed that the decolorization rate remains unaffected by the concentration of H₂O₂ (ranging from 2.35 × 10⁻⁵ to 4.70 × 10⁻⁵ mol) and the catalyst mass (ranging from 20 to 40 mg). In other words, under these conditions, reactions 9-20 would not undergo changes in velocity, thereby preserving process efficiency.

Electrochemical properties of mixed oxide

To investigate the electrochemical behavior of the mixed oxide, a study of this composite was conducted at different potential scan rates (10 to 150 mV s⁻¹) using the cyclic voltammetry technique in a 1 mol L⁻¹ KOH electrolyte solution (Figure 6).

Upon examination of the voltammograms, it was observed that the oxidation potential (anodic peaks) shifted towards more positive values as the potential scan rate increased, accompanied by an increase in the magnitude of the anodic current. Furthermore, cathodic peaks were also detected during the reverse potential scan, indicating the reversible nature of the mixed oxide behavior.⁶⁵

Based on the data obtained from this study, a logarithmic graph of the anodic peak current (log I_{ap}) plotted against the logarithm of the potential scan rate (log ν) was constructed, as illustrated in Figure S8a (SI section). Analysis of the results revealed a linear relationship between log I_{ap} and log ν. The slope of the line, approximately 0.49, indicates that the oxidation process is diffusion-controlled, as values around 0.50 suggest diffusion control, while values of 1.0 indicate adsorption control. The observed linearity between the anodic peak current (I_{ap}) and the square root of the scan rate (ν^{1/2}) (Figure S8b, SI section) confirms the diffusion-controlled nature of the system.⁶⁶ The same graphs constructed for the cathodic peak (cp) also demonstrate a linear correlation between the parameters log I_{cp} and log ν (Figure S8c, SI section) and between I_{cp}

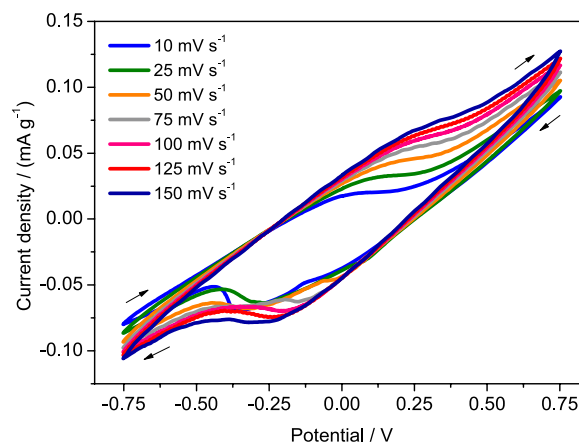


Figure 6. Cyclic voltammetry of the mixed oxide at different scan rates of 10, 25, 50, 75, 100, 125 and 150 mV s⁻¹.

and ν^{1/2} (Figure S8d, SI section). Therefore, the cathodic process is also diffusion-controlled, but only starting from a scan rate of 25 mV s⁻¹.

The presence of the redox peaks observed in Figure 6 can be related to the Fe³⁺/Fe²⁺ redox reactions and indicate that the process is governed by faradaic oxidation-reduction reactions, exhibiting pseudocapacitor behavior.^{67,68} Galvanostatic charge/discharge measurements were conducted to analyze the pseudocapacitive performance of the mixed oxide. The specific capacitance is derived from the galvanostatic discharge curves (Figure 7a) using the following equation (equation 21).

$$C = \frac{I \Delta t}{m \Delta V} \quad (21)$$

where C is the specific capacitance (F g⁻¹), I is the current (A), Δt is the discharging time (s), m is the mass of the active material (g) and ΔV is the potential window (V).

In the first cycle, the material exhibited a specific capacitance of 107.64 F g⁻¹, reaching its maximum value of 286.60 F g⁻¹ after 15 cycles and stabilizing at 87.16 F g⁻¹, for current densities of 0.7 A g⁻¹, as shown in Figure 7b. The results can be attributed to the excellent electrode-electrolyte contact, ensuring optimal utilization of the electrode's effective surface area and active sites by the electrolyte.⁶⁷

The energy density (equation 22) and power density (equation 23) were calculated through the following equations.

$$E = \frac{C (\Delta V)^2}{2 \times 3.6} \quad (22)$$

$$P = \frac{3600 E}{\Delta t} \quad (23)$$

where E is the energy density expressed in (Wh kg⁻¹) and P is the power density expressed in (W kg⁻¹).

The mixed oxide exhibited energy density of 27.24 Wh kg⁻¹ with power density of 524.41 W kg⁻¹ after stabilization, which showed the great application prospect for energy storage. The electrochemical energy storage performance of the mixed oxide was superior than those reported in literature such as ZnO/MnOx (16 Wh kg⁻¹ at 225 W kg⁻¹),⁶⁹ ZnMn₂O₄ (25.51 Wh kg⁻¹ at 399.98 W kg⁻¹),⁷⁰ MnO₂/Fe₂O₃ (15.58 Wh kg⁻¹ at 399 W kg⁻¹),⁷¹ NiCo₂S₄/Fe₂O₃ (25 Wh kg⁻¹ at 54 W kg⁻¹).⁷²

The mixed oxide has promising electrochemical characteristics for application in pseudocapacitors, as it presents high specific capacitance, energy density, power density, charge efficiency and reversibility in charge/discharge cycles (93.4% after 100 cycles).

Conclusions

The mixed oxide composed of SiO₂, ZnO, Fe₂O₃, and ZnFe₂O₄ had irregular shape and a surface with adhered fragments. Of the three variables studied, pH was the most significant for increasing MB decolorization. The mixed oxide showed better catalytic performance (about 96% efficiency) in the decolorization of 1.56 × 10⁻⁶ mol MB under the following conditions: 2.35 × 10⁻⁵ mol H₂O₂, 20 mg of mixed oxide, pH 3, 30 min, and UV solar irradiation. The zero-order rate constant was 0.0333 mg L⁻¹ min⁻¹ and the half-life was 15.85 min for the system containing H₂O₂ and mixed oxide; these values were 6 times higher than that of the system containing MB and H₂O₂ only. Under optimal conditions, the mixed oxide proved to be reusable for four successive catalytic cycles, with a mean efficiency of 96%, indicating high stability. This study demonstrates that effective photocatalysts can be prepared by a sustainable method using mining industry tailings and spent alkaline batteries for application in MB decolorization

with solar irradiation. Furthermore, by applying the optimal conditions, the efficiency of the process is guaranteed and costs are minimized. In addition, the sustainable mixed oxide is a bifunctional material that can also be applied as an energy storage device due to its electrochemical characteristics, including high specific capacitance (87.16 F g⁻¹), high energy density (27.24 Wh kg⁻¹) at 524.41 W kg⁻¹ of power density, and excellent reversibility in charge/discharge cycles (93%).

Supplementary Information

Supplementary information (sample collection points for mining tailings, weather conditions on the day of the photocatalytic optimization, experimental conditions of the 2³ full factorial design, adsorption study of the mixed oxide, XRD of the alkaline battery anode and of the silt fraction, decolorization efficiency of MB, Pareto chart, pH optimization, and dependence of anodic and cathodic current of the scan rate) is available free of charge at <http://jbcs.sbq.org.br> as PDF file.

Acknowledgments

The authors thank the CAPES, Finance Code 001), CNPq for the financial support. We also thank LabPetro (UFES, Brazil) for performing XRD (Technical Cooperation Agreements No. CT-Infra 01/2007, FINEP 0202/08), and ICP-OES measurements and the Laboratório de Ultraestrutura Celular Carlos Alberto Redins (LUCCAR/UFES) for conducting SEM, EDX, and TEM analyses.

Author Contributions

Luma B. Magnago was responsible for the conceptualization, data curation, formal analysis, investigation, methodology, visualization, writing (original draft, review and editing); Fernando S. Betim, Jenifer

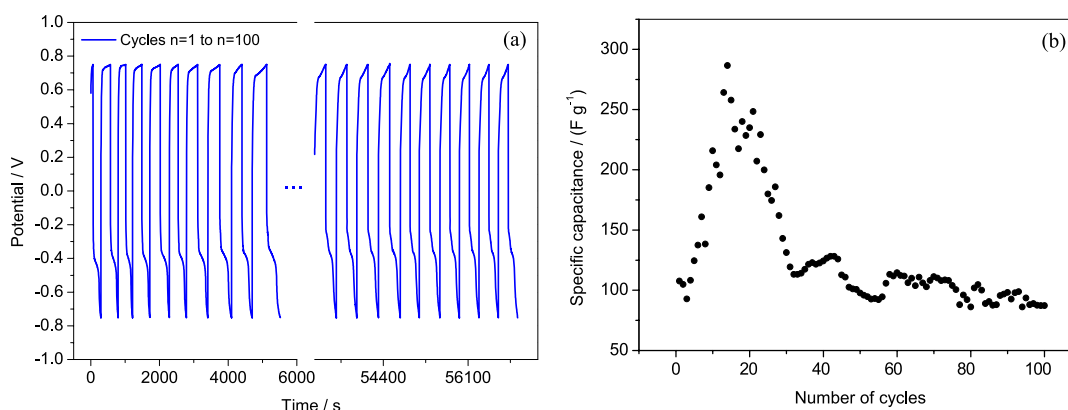


Figure 7. (a) Galvanostatic charge/discharge curves for the mixed oxide (cycles n = 1 to n = 100), (b) specific capacitance behavior as a function of the number of cycles.

R. Almeida, Mayra N. Moura, Edson L. D. Carvalho and Vitor M. Leal for data curation, investigation, methodology, visualization, writing (original draft, review and editing); Sandra A. D. Ferreira, Maria F. F. Lelis and Marcos B. J. G. de Freitas were responsible for the conceptualization, investigation, methodology, resources, supervision, project administration, visualization, writing (original draft, review and editing).

References

1. Presidência da República Casa Civil; Lei No. 12.305, de 02 de agosto de 2010, Institui a *Política Nacional de Resíduos Sólidos*; Diário Oficial da União (DOU), Brasília, Brazil, 2010. [Link] accessed in November 2023
2. Dutta, T.; Kim, K.-H.; Deep, A.; Szulejko, J. E.; Vellingiri, K.; Kumar, S.; Kwon, E. E.; Yun, S.-T.; *Renewable Sustainable Energy Rev.* **2018**, *82*, 3694. [Crossref]
3. Mylarappa, M.; Lakshmi, V. V.; Mahesh, K. R. V.; Nagaswarupa, H. P.; Raghavendra, N.; *Mater. Today: Proc.* **2019**, *9*, 256. [Crossref]
4. Smith, W. N.; Arutunian, M.; Swoffer, S.; *US pat. 8728419B1*, **2014**.
5. Resíduos eletrônicos no Brasil-2021, https://greeneletron.org.br/download/RELATORIO_DE_DADOS.pdf, accessed in November 2023.
6. Liu, C.-W.; Lin, C.-H.; Fu, Y.-P.; *J. Am. Ceram. Soc.* **2007**, *90*, 3349. [Crossref]
7. Sayilgan, E.; Kukrer, T.; Yigit, N. O.; Civelekoglu, G.; Kitis, M.; *J. Hazard. Mater.* **2010**, *173*, 137. [Crossref]
8. Gu, F.; Zhang, W.; Guo, J.; Hall, P.; *Sci. Total Environ.* **2019**, *649*, 172. [Crossref]
9. Provazi, K.; Campos, B. A.; Espinosa, D. C. R.; Tenório, J. A. S.; *Waste Manage.* **2011**, *31*, 59. [Crossref]
10. Sistema Estadual de Meio Ambiente e Recursos Hídricos Fundação Estadual do Meio Ambiente; *Inventário de Resíduos Sólidos da Mineração Ano Base 2017*; Belo Horizonte, 2018. [Link] accessed in November 2023
11. Quadra, G. R.; Roland, F.; Barros, N.; Malm, O.; Lino, A. S.; Azevedo, G. M.; Thomaz, J. R.; Andrade-Vieira, L. F.; Praça-Fontes, M. M.; Almeida, R. M.; Mendonça, R. F.; Cardoso, S. J.; Guida, Y. S.; Campos, J. M. S.; *Chemosphere* **2019**, *215*, 753. [Crossref]
12. Segura, F. R.; Nunes, E. A.; Paniz, F. P.; Paulelli, A. C. C.; Rodrigues, G. B.; Braga, G. U. L.; Pedreira Filho, W. R.; Barbosa Jr., F.; Cerchiaro, G.; Silva, F. F.; Batista, B. L.; *Environ. Pollut.* **2016**, *218*, 813. [Crossref]
13. Laudo Técnico Preliminar: *Impactos Ambientais Decorrentes do Desastre Envolvendo o Rompimento da Barragem de Fundão, em Mariana, Minas Gerais*, http://www.ibama.gov.br/phocadownload/barragemdefundao/laudos/laudo_tecnico_preliminar_ibama.pdf, accessed in November 2023.
14. Parul; Kaur, K.; Badru, R.; Singh, P. P.; Kaushal, S.; *J. Environ. Chem. Eng.* **2020**, *8*, 103666. [Crossref]
15. Far, H.; Hamici, M.; Brihi, N.; Haddadi, K.; Boudissa, M.; Chihi, T.; Fatmi, M.; *J. Mater. Res. Technol.* **2022**, *19*, 1944. [Crossref]
16. Zhu, D.; Zhou, Q.; *Environ. Nanotechnol., Monit. Manage.* **2019**, *12*, 100255. [Crossref]
17. Pattnaik, A.; Sahu, J. N.; Poonia, A. K.; Ghosh, P.; *Chem. Eng. Res. Des.* **2023**, *190*, 667. [Crossref]
18. Shah, R. K.; *Arabian J. Chem.* **2023**, *16*, 104444. [Crossref]
19. Subaihi, A.; Naglah, A. M.; *Arabian J. Chem.* **2022**, *15*, 103613. [Crossref]
20. Adekunle, A. S.; Oyekunle, J. A. O.; Durosinmi, L. M.; Saheed, O.; Ajayeoba, T. A.; Akinyele, O. F.; Elugoke, S. E.; Oluwafemi, O. S.; *Nano-Struct. Nano-Objects* **2021**, *28*, 100804. [Crossref]
21. Haseena, S.; Shanavas, S.; Ahamad, T.; Alshehri, S. M.; Baskaran, P.; Duraimurugan, J.; Acevedo, R.; Khan, M. A. M.; Anbarasan, P. M.; Jayamani, N.; *J. Environ. Chem. Eng.* **2021**, *9*, 104996. [Crossref]
22. Waghchaure, R. H.; Adole, V. A.; Jagdale, B. S.; *Inorg. Chem. Commun.* **2022**, *143*, 109764. [Crossref]
23. Isa, E. D. M.; Jusoh, N. W. C.; Hazan, R.; Shamel, K.; *Environ. Sci. Pollut. Res.* **2021**, *28*, 5774. [Crossref]
24. Smazna, D.; Shree, S.; Polonskyi, O.; Lamaka, S.; Baum, M.; Zheludkevich, M.; Faupel, F.; Adelung, R.; Mishra, Y. K.; *J. Environ. Chem. Eng.* **2019**, *7*, 103016. [Crossref]
25. Harijan, D. K. L.; Gupta, S.; Ben, S. K.; Srivastava, A.; Singh, J.; Chandra, V.; *Phys. B* **2022**, *627*, 413567. [Crossref]
26. Li, Y.; Wei, G.; Shao, L.; Li, Z.; Yu, F.; Liu, J.; Yang, X.; Lu, Q.; Li, A.; Huang, Y.; Zhang, L.; *J. Cleaner Prod.* **2019**, *207*, 717. [Crossref]
27. Angelin, M. D.; Rajkumar, S.; Ravichandran, A. T.; Merlin, J. P.; *J. Phys. Chem. Solids* **2022**, *161*, 110486. [Crossref]
28. Kahimbi, H.; Jeong, J.-M.; Kim, D. H.; Kim, J. W.; Choi, B. G.; *Solid State Sci.* **2018**, *83*, 201. [Crossref]
29. Hassan, I. U.; Salim, H.; Naikoo, G. A.; Awan, T.; Dar, R. A.; Arshad, F.; Tabidi, M. A.; Das, R.; Ahmed, W.; Asiri, A. M.; Qurashi, A.; *J. Saudi Chem. Soc.* **2021**, *25*, 101228. [Crossref]
30. Maksoud, M. I. A. A.; Fahim, R. A.; Shalan, A. E.; Elkodous, M. A.; Olojede, S. O.; Osman, A. I.; Farrell, C.; Al-Muhtaseb, A. H.; Awed, A. S.; Ashour, A. H.; Rooney, D. W.; *Environ. Chem. Lett.* **2021**, *19*, 375. [Crossref]
31. Rouibah, K.; Akika, F.-Z.; Rouibah, C.; Boudermine, H.-R.; Douafer, S.; Boukerche, S.; Boukerche, G.; Benamira, M.; *Inorg. Chem. Commun.* **2023**, *148*, 110361. [Crossref]
32. Sangaiya, P.; Jayaprakash, R.; Shkir, M.; Ashraf, I. M.; Gedi, S.; *Inorg. Chem. Commun.* **2022**, *144*, 109852. [Crossref]
33. Ibrahim, Y.; Abdullah, A. H.; Rashid, S. A.; Muhamad, E. N.; *Opt. Mater.* **2023**, *136*, 113371. [Crossref]
34. ABNT NBR 10007: *Amostragem de Resíduos Sólidos*, 2nd ed.; ABNT: Rio de Janeiro, Brazil, 2004. [Link] accessed in November 2023

35. Figueiredo, M. D.; Lameiras, F. S.; Ardisson, J. D.; Araujo, M. H.; Teixeira, A. P. C.; *Integr. Environ. Assess. Manage.* **2020**, *16*, 636. [Crossref]
36. ABNT NBR 10004: *Resíduos Sólidos-Classificação*, 2nd ed.; ABNT: Rio de Janeiro, Brazil, 2004. [Link] accessed in November 2023
37. Teixeira, P. C.; Donagemma, G. K.; Fontana, A.; Teixeira, W.G. In *Manual de Métodos de Análise de Solo*, 3rd ed.; Embrapa: Brasília, Brazil, 2017. [Link] accessed in November 2023
38. *Statistica*, version 11.0; StatSoft Inc., Tulsa, OK, USA, 2012.
39. Buzatu, T.; Popescu, G.; Birloaga, I.; Săceanu, S.; *Waste Manage.* **2013**, *33*, 699. [Crossref]
40. Belardi, G.; Ballirano, P.; Ferrini, M.; Lavecchia, R.; Medici, F.; Piga, L.; Scoppettuolo, A.; *Thermochim. Acta* **2011**, *526*, 169. [Crossref]
41. Valdez, I. V.; Almeida, M. F.; Dias, J. M.; *J. Environ. Manage.* **2022**, *321*, 115979. [Crossref]
42. Cabral, M.; Poderosa, F.; Margarido, F.; Nogueira, C. A.; *Environ. Technol.* **2013**, *34*, 1283. [Crossref]
43. Almeida, M. F.; Xará, S. M.; Delgado, J.; Costa, C. A.; *Waste Manage.* **2006**, *26*, 466. [Crossref]
44. Almeida, C. A.; de Oliveira, A. F.; Pacheco, A. A.; Lopes, R. P.; Neves, A. A.; de Queiroz, M. E. L. R.; *Chemosphere* **2018**, *209*, 411. [Crossref]
45. Welter, N.; Leichtweis, J.; Silvestri, S.; Sánchez, P. I. Z.; Mejía, A. C. C.; Carissimi, E.; *J. Alloys Compd.* **2022**, *901*, 163758. [Crossref]
46. Cherpin, C.; Lister, D.; Dacquait, F.; Liu, L.; *Materials* **2021**, *14*, 2557. [Crossref]
47. Sriprom, P.; Krobthong, W.; Assawasaengrat, P.; *Energy Rep.* **2020**, *6*, 731. [Crossref]
48. Yildiz, S.; Canbaz, G. T.; Kaya, S.; Maslov, M. M.; *J. Mol. Struct.* **2023**, *1277*, 134833. [Crossref]
49. Azizi, A.; Moghaddam, M. R. A.; Maknoon, R.; Kowsari, E.; *J. Hazard. Mater.* **2015**, *299*, 343. [Crossref]
50. Vianna, V. B.; Tôrres, A. R.; *Quim. Nova* **2008**, *31*, 1353. [Crossref]
51. Conselho Nacional do Meio Ambiente (CONAMA); Resolução No. 430, de 13 de maio 2011, Dispõe sobre as *Condições e Padrões de Lançamento de Efluentes*; Diário Oficial da União (DOU), Brasília, No, 92, de 16/05/2011, p. 89. [Link] accessed in November 2023
52. Magnago, L. B.; Rocha, A. K. S.; Pegoretti, V. C. B.; Ferreira, S. A. D.; Lelis, M. F. F.; Freitas, M. B. J. G.; *Ionics* **2019**, *25*, 2361. [Crossref]
53. Rocha, A. K. S.; Magnago, L. B.; Santos, J. J.; Leal, V. M.; Marins, A. A. L.; Pegoretti, V. C. B.; Ferreira, S. A. D.; Lelis, M. F. F.; Freitas, M. B. J. G.; *Mater. Res. Bull.* **2019**, *113*, 231. [Crossref]
54. Moura, M. N.; Barrada, R. V.; Almeida, J. R.; Moreira, T. F. M.; Schettino, M. A.; Freitas, J. C. C.; Ferreira, S. A. D.; Lelis, M. F. F.; Freitas, M. B. J. G.; *Chemosphere* **2017**, *182*, 339. [Crossref]
55. Gerbaldo, M. V.; Marchetti, S. G.; Mendoza, S. M.; Elias, V. R.; Mendieta, S. N.; Crivello, M. E.; *Top. Catal.* **2022**, *65*, 1419. [Crossref]
56. Motamedi, M.; Yerushalmi, L.; Haghighat, F.; Chen, Z.; *Chemosphere* **2022**, *296*, 133688. [Crossref]
57. Gao, S.; Feng, D.; Chen, F.; Shi, H.; Chen, Z.; *Colloids Surf., A* **2022**, *648*, 129282. [Crossref]
58. Silva, E. N.; Brasileiro, I. L. O.; Madeira, V. S.; Farias, B. A.; Ramalho, M. L. A.; Rodríguez-Aguado, E.; Rodríguez-Castellón, E.; *J. Environ. Chem. Eng.* **2020**, *8*, 104132. [Crossref]
59. Ivanets, A.; Prozorovich, V.; Sarkisova, V.; Roshchina, M.; Grigoraviciute-Puroniene, I.; Zarkov, A.; Kareiva, A.; Masindi, V.; Wang, C.; Srivastava, V.; Sillanpää, M.; *Ceram. Int.* **2021**, *47*, 29786. [Crossref]
60. Rini, N. P.; Istiqomah, N. I.; Sunarta; Suharyadi, E.; *Case Stud. Chem. Environ. Eng.* **2023**, *7*, 100301. [Crossref]
61. Casbeer, E.; Sharma, V. K.; Li, X.-Z.; *Sep. Purif. Technol.* **2012**, *87*, 1. [Crossref]
62. Yu, X.; Somoza-Tornos, A.; Graells, M.; Pérez-Moya, M.; *Sci. Total Environ.* **2020**, *743*, 140402. [Crossref]
63. Nachimuthu, S.; Thangavel, S.; Kannan, K.; Selvakumar, V.; Muthusamy, K.; Siddiqui, M. R.; Wabaidur, S. M.; Parvathiraja, C.; *Chem. Phys. Lett.* **2022**, *804*, 139907. [Crossref]
64. Zhu, Y.; Zhu, R.; Xi, Y.; Zhu, J.; Zhu, G.; He, H.; *Appl. Catal., B* **2019**, *255*, 117739. [Crossref]
65. Pletcher, D.; Greef, R.; Peat, R.; Peter, L. M.; Robinson, J.; *Instrumental Methods in Electrochemistry*, 1st ed.; Elsevier: Woodhead Publishing Limited, 2001. [Link] accessed in November 2023
66. Chen, G. Z.; *Prog. Nat. Sci.: Mater. Int.* **2021**, *31*, 792. [Crossref]
67. Askari, M. B.; Salarizadeh, P.; Seifi, M.; Zadeh, M. H. R.; Bartolomeo, A. D.; *J. Alloys Compd.* **2021**, *860*, 158497. [Crossref]
68. Rajesh, J. A.; Min, B.-K.; Kim, J.-H.; Kim, H.; Ahn, K.-S.; *J. Electrochem. Soc.* **2016**, *163*, A2418. [Crossref]
69. Samuel, E.; Joshi, B.; Kim, Y.-I.; Aldalbahi, A.; Rahaman, M.; Yoon, S. S.; *ACS Sustainable Chem. Eng.* **2020**, *8*, 3697. [Crossref]
70. Gao, P.; Shen, B.; Zhao, P.; Shi, G.; Zhao, X.; *J. Power Sources* **2023**, *577*, 233231. [Crossref]
71. Phakkhawan, A.; Suksangrat, P.; Srepusharawoot, P.; Ruangchai, S.; Klangtakai, P.; Pimanpang, S.; Amornkitbamrung, V.; *J. Alloys Compd.* **2022**, *919*, 165702. [Crossref]
72. Guo, R.; Dang, L.; Liu, Z.; Lei, Z.; *Colloids Surf., A* **2020**, *602*, 125110. [Crossref]

Submitted: August 12, 2023

Published online: November 16, 2023